EXPERIMENTAL AND NUMERICAL ANALYSIS FOR THE DRY PATCH AND THERMAL STRESS OF ONE HEATING SURFACE

by

Yijun ZHANG[a], Yun GUO[a*], and Jinman ZHOU[b]

[a]School of nuclear science and technology, University of Science and Technology of China, Hefei, China
[b]Nuclear Power Institute of China, Chengdu, China

Original scientific paper
https://doi.org/10.2298/TSCI240324169Z

In this study, an experiment to explore the surface temperature rise of an artificial dry patch at different heating powers was done. Then under specific sizes of the dry patches, the influences of these factors on thermal stress were thoroughly investigated through sensitivity analyses of factors such as the thickness of the heated wall surface, the location of the dry patch, and the thermal conductivity of the heating surface. It is found that in the case of CHF occurrence, even though the local maximum temperature inside the dry patch is much lower than the melting point of the material, the thermal stress caused by the dry patch exceeds the yield strength of the material, which triggers irreversible plastic deformation. Therefore, the heated wall fracture caused by thermal stress will occur prior to wall melting. At the same time, this study also found that changing the thickness of the stainless steel base plate and the thermal conductivity of the material both affect the maximum temperature in the dry patch region. Reducing the thickness of the heating plate makes the temperature in the dry patch region increase, which leads to a dramatic increase in the thermal stresses inside the material. Increasing the thermal conductivity of the material can flatten the temperature field, and the equivalent stresses also decrease.

Key words: *critical heat flux, dry patch, thermal stress*

Introduction

The CHF is a long-standing research topic owing to its rich behavior and many applications, a unified theoretical explanation has not yet been developed. Among the existing theoretical models, the hydrodynamic instability model, the microlayer dry-out theory, and the dry patch theory are considered to describe CHF better within a certain range. The hydrodynamic instability theory, first proposed by Kutateladze and Zuber [1, 2], suggests that the up-flow steam stops the downflow liquid, triggering CHF, when the difference in velocities between the vapor and liquid phases is greater than a critical value. In other words, the wall surface is no longer wetted by the liquid phase, leading to a decrease in the cooling effect, which triggers a temperature increase. According to the heat flux correlation of the Kutateladze-Zuber model,

*Corresponding author, e-mail: guoyun79@ustc.edu.cn

the model suggests that the CHF depends only on the physical properties of the fluid and is independent of the material properties of the boiling surface. The microlayer dry out model proposed by Haramura and Katto [3], on the other hand, assumes that CHF occurrence requires the complete evaporation of the liquid microlayer under the bubble before the bubble departure. In addition, Ha and No [4, 5] proposed the concept of unquenchable and quenchable dry patches at high heat flux, where the surrounding liquid is unable to wet the dry patch when the number of surrounding bubbles exceeds a certain critical value, hindering heat removal and eventually leading to the occurrence of CHF.

In past studies, CHF has been regarded as a hydrodynamic or bubble-dynamic phenomenon, and most of the empirical correlations are based on liquid-side parameters independent of the heated wall condition. Obviously, if the bubbles have a strong relationship with CHF the surface condition cannot be ignored. Many studies have emphasized that CHF may be closely related to the properties of the heated wall surface. For example, Tachibana [6] *et al.* investigated the effect of heater thermal properties on CHF, Costello and Frea [7] demonstrated that CHF increased with increasing deposits by varying the thickness of deposits on the cylinders. Howard and Mudawar [8] investigated the effect of different arrangement directions of the heater on CHF, and found that CHF has a unique mechanism of occurrence. References [9, 10] also showed that the occurrence of CHF is closely related to dry patches on the heated wall. Gong *et al.* [11] observed the evolution of bubbles and dry patches in the boiling liquid film by using a high-speed camera, and found that the large dry patches leading to CHF propagate from the edge of the heated zone to the center. They concluded that the critical thickness depends on the evaporation rate or heat flux and observed a stable unquenchable dry patch by thinning the liquid film. Chu *et al.* [12, 13,] developed techniques for the simultaneous display of bubble growth and dry patch growth using visualization techniques. The careful observation of the water boiling heat transfer process by these two techniques focused on the dynamics of the unquenchable dry patch. They proposed that as bubbles leave the wall, a small residual drying zone is left behind at the wall, which is surrounded by strong bubble nucleation, and the rapid expansion of the dry patch triggers the growth of the unquenchable dry patch, which leads to the CHF. Although these techniques succeeded in explaining the triggering mechanism of the CHF and provided good physical insights, they did not measure the localized temperature distributions within the actual dry patch region, which may be a key parameter in the study of nuclear-boiling heat transfer stability.

Dry patch model

A study by Chu *et al.* [13] found that during the process of generating dry spots, aggregation occurs between these dry spots to form larger dry patches. Further in-depth studies have carefully categorized dry spots into hot and cold spots based on the work of Bernardin *et al.* [14]. The presence of dry spots is greatly dependent on the superheat of the wall, which determines bubble nucleation and bubble residence time. When a bubble is created, a very thin layer of liquid, known as a liquid microlayer, forms below the bubble. If the presence of other bubbles in the surrounding area prevents the liquid from entering the microlayer under the center bubble, this microlayer quickly dries out, resulting in the formation of a dry spot. As the heat flux increases, the bubbles polymerize and begin to turn into mushroom-shaped bubbles, while the dry spots aggregate to form dry patches. When the mushroom-shaped bubbles leave the wall due to buoyancy, some of the dry patches under the bubbles are completely rewetted, called quenchable dry patches, and some are not rewetted, called unquenchable dry patches. Therefore, after an unquenchable dry patch is created, the departure of bubbles will not affect

the dry patch, and the temperature inside the dry patch will continue to rise. Throughout the cycle, even when the mushroom bubbles are detached from the wall, the unquenchable dry patches remain and expand with a further increase in wall temperature, eventually triggering CHF.

On this basis, Choi and No [15] proposed two conditions for generating the formation of an unquenchable dry patch with a critical size:

Hydrodynamic criterion: The number of dry spots must reach a critical level where all dry spots are in contact with each other, and dry spots larger than the critical number are needed to polymerize with each other to form dry patches.

Thermal Criteria: The peripheral temperature of the dry patch needs to reach the Leidenfrost temperature. The Leidenfrost temperature is regarded as the peripheral temperature for an unquenchable dry patch. When the temperature around the dry patch reaches the peripheral temperature, the liquid cannot come into contact with the heater, making it impossible for the dry patch to rewet and remain dry.

For metals, the Leidenfrost temperature of water is about 173-200 °C [16]. However, it has been shown that the temperature of the dry patch at the onset of CHF is much lower than the Leidenfrost temperature, with specific experiments observing critical temperatures commonly around 150 °C [17-19]. In the calculations, the size of the dry patch that satisfies the condition of an unquenchable dry patch is controlled to ensure that its temperature is higher than the Leidenfrost temperature. In addition, the distribution of nucleation sites was described by introducing the Poisson distribution equation. Finally, based on the assumption of an unquenchable dry patch, a computational model for generating the critical size of an unquenchable dry patch is proposed.

In pool boiling experiments, there is no accurate experimental value for the diameter of the unquenchable dry patch. In current visualization experiments, the heated wall material is often chosen to be a light-transmitting sapphire liner to facilitate direct observation of the unquenchable dry patch, which leads to a large difference between the experimental heated wall material and the metal material used in real engineering. The size of the unquenchable dry patch is related to the material properties of the heated wall. According to [10], the diameter of the unquenchable dry patch is estimated by calculating the critical liquid-solid contact temperature, such as copper heated surfaces, the diameter of the unquenchable dry patch is around 10-23 mm, and nickel metal surfaces, the diameter of the unquenchable dry patch is around 2.25 mm.

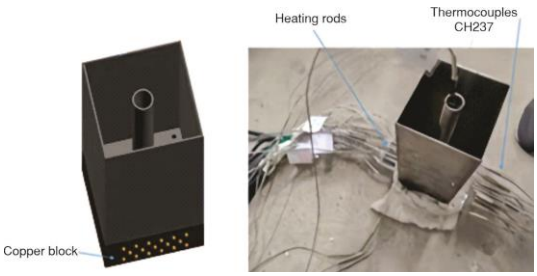

Figure 1. Diagram of the experimental equipment

Experiment

Experimental equipment

Figure 1 illustrates a schematic diagram of a pool boiling experimental set-up. The structure and thermocouple arrangement are shown in fig. 2. At the bottom of the device is a heating body copper block with dimensions of 110.0 mm × 110.0 mm × 50.0 mm. The upper end of the copper block is equipped with a stainless steel box measuring 110.0 mm × 110.0 mm × 200.0 mm. A stainless steel tube, with an inner diameter of 10.0 mm, height of 200.0 mm, and a thickness of 2.0 mm, is welded at the center of the bottom. The

thermocouples numbered CH237 are positioned at the center of the circle to measure the local temperature. The outside of the whole equipment was wrapped with a 6 cm thick asbestos for insulation. Other thermocouples were inserted through the asbestos layer into the temperature measurement holes of the copper block and fixed in the simulated drying zone.

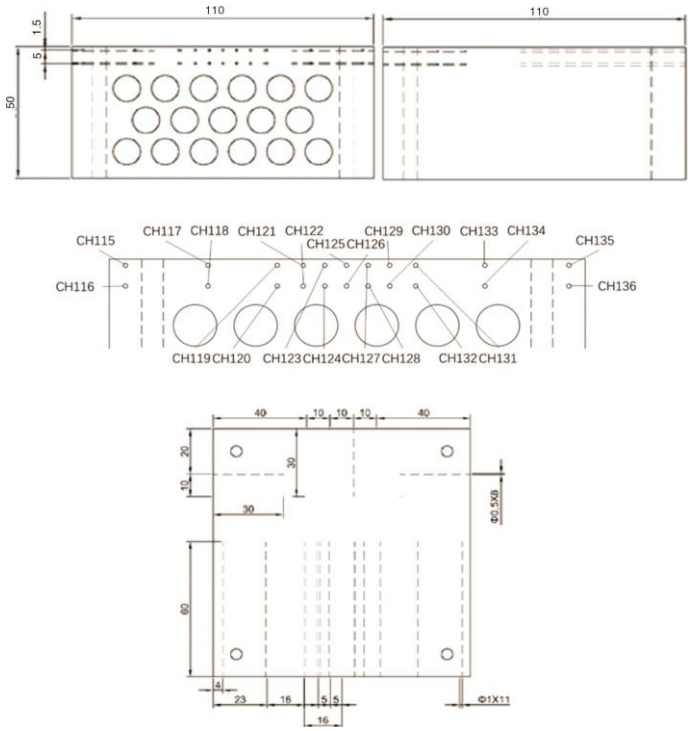

Figure 2. The arrangement of thermocouples

In the experiment, the body of the copper block was heated through 17 heating tubes and the bottom of the stainless-steel box was heated by the copper block. A sufficient amount of water was added to the stainless steel box on the copper block and a small amount of water was added to the simulated drying zone and heated to boiling. The heating power was then adjusted by regulating the output voltage of the regulator to increase the heat flux at the bottom of the box gradually. Due to the high requirements for direct measurement of the internal stresses in the material, monitoring of the temperature at the center of the heat transfer deterioration zone was used. Temperature data acquisition was carried out by means of a Keithley Model 7708 40-channel data acquisition card and a Keithley Model 2750 digital multimeter to monitor the temperature field of the copper block, especially the rise of the wall temperature after the water in the center tube was drained. In fact, this experiment is not a real CHF test. The Heat transfer deteriorates due to the artificially drying of water instead of bubbling. The experiment done here is to illustrate the accuracy of the latter calculation model of the dry patch temperature.

Experimental data

Figure 3 shows the results of three cases by CH237 thermocouple measurements. Using the thermocouples in the body of the copper block, the heat flux transferred to the bottom of the stainless steel box can be obtained. In the first test, the average bottom heat flux was

approximately 0.520 W/mm². However, when a larger heat source was applied to the copper block body, due to the thicker body and higher internal temperature of the copper block, the maximum temperature inside the block easily exceeded the melting point. So in Cases 2 and 3, the average bottom heat fluxes were around 0.394 W/mm² and 0.300 W/mm². The experiment is not a direct simulation of CHF. The purpose of the experiment is to validate the temperature rise pattern in the center of the dry patch, and thus compare it with the simulated data to verify the accuracy of the model.

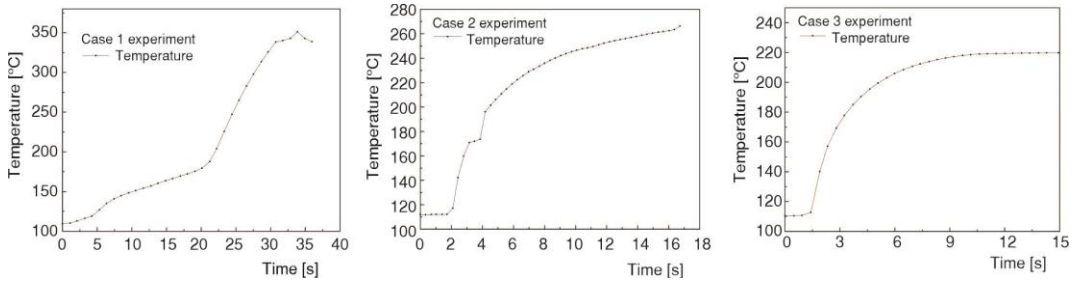

Figure 3. Temperature curves at the center point of the artificial dry patch in Cases 1-3

It should be further noted that in Cases 1-3, different rates of power increase resulted in differences in the dry patch evaporation process. In Case 1, the water in the center of the circular tube was gradually burnt dry, a relatively slow process. In this case, the temperature of the heating surface in the center of the round tube started to rise slowly and the temperature rise curve showed a relatively smooth characteristic. However, when the water was completely evaporated, the temperature rise curve became steeper and the rate of temperature rise increased significantly. In contrast, in Cases 2 and 3, the rate of increasing power was faster. The formation of dry patches was simulated by artificially draining the water in the round tube. In such a way that there was no need to wait for the gradual evaporation process of the water. As a result, once the water in the round tube is completely drained, the temperature immediately starts to rise rapidly and the temperature rise curve shows a sharp upward trend.

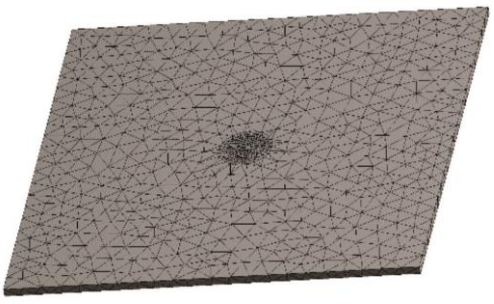

Figure 4. Stainless steel plate as well as dry patch model drawing

Simulation

Model

When using ANSYS Workbench for the simulation the model is simplified in order to focus on the temperature situation at the boiling surface. Only stainless steel bases are considered in geometric modeling. The copper block is looked as a homogeneous surface heat source for the stainless steel pool. In the simulation, the wetting zone by adding a sufficient amount of water to the stainless-steel box was modeled, while a small amount of water was added to the simulated drying zone and heated to boiling. The model is shown in fig 4. The dimensions of the stainless steel base plate are 110.0 mm × 110.0 mm × 2 mm. Since the simulation process is more concerned with the temperature and stress distribution in the region where the dry patch is located on the boiling surface, the dry

patch as well as the surrounding region is refined appropriately with the number of nodes in the model being 75580 and the number of elements being 41500.

The state before the simulated drying zone evaporates to dryness was set as a steady state, at which time the heat transfer coefficient was kept the same as that of the wet surface. Once the simulated dry zone is evaporated completely, the dry patch area was set as an adiabatic surface because the heat transfer coefficient of the dry patch located in the center of the surface is significantly lower than that of the surrounding nuclear boiling zone. In the experiments, the outer wall surfaces of stainless steel and copper blocks were wrapped with asbestos, so the simulation process considered that the stainless steel only dissipated heat through the boiling surface, and the other walls were adiabatic. The heat transfer coefficient of the boiling surface was set to the value of h measured in the experiment [20], where the convective heat transfer coefficient varied between 28000 and 33000, and was uniformly taken to be 30000 in this calculation. Transient calculations were performed next, where the heat was applied from the lower side of the surface and transferred to the upper surface through the heater, which had a thickness of 2 mm. The stainless steel material parameters used in this experiment are shown in tab. 1.

Table 1. The stainless steel material parameters

Item	Value
Density	7750 kg/m^2
Coefficient of thermal expansion	1.7×10^{-5} K^{-1}
Young's modulus	1.93×10^{11} Pa
Poisson's rRatio	0.31
Tensile yield strength	207 MPa
Compressive yield strength	207 MPa
Tensile ultimate strength	586 MPa
Isotropic thermal conductivity	15.1 W/mK
Specific heat	480 J/kgK

Dry patch

During the experiment, the stainless steel tube wall is in contact with water on the outside and air on the inside, and the thickness of the stainless steel tube wall is 2 mm. Some heat will be transferred into the air through the tube. However, the heat transfer is certainly not as strong as the external nuclear boiling. It looks like the dry zone was expanded. This factor was taken into account when predicting the dry patch radius of the actual dry patch, which was set to 5 mm, 6 mm, and 7 mm for simulations, respectively.

The simulation results are shown in fig. 5. In case 1, the maximum wall temperature decreases rapidly after reaching 360 °C. It is hypothesized that the actual steady-state maximum wall temperature will not exceed 360 °C. By comparing the steady-state maximum temperatures of different sizes of dry patches with radio of 5 mm, 6 mm, and 7 mm, we believe that it is more accurate to use a 6 mm dry patch, and then the 6 mm dry patch modeling was also used to simulate Cases 2 and 3. The corresponding temperature distributions were obtained, as shown in fig. 6. The difference is caused by heat loss. Some heating power is released to the surroundings from the center circular tube and the surface of the surrounding water by convection and radiation. These factors actually reduced the rate of temperature rise and maximum temperature in the center, which led to a prolongation of the temperature rise phenomenon. Now, the method can be used to investigate some interesting physics related to the dry patch.

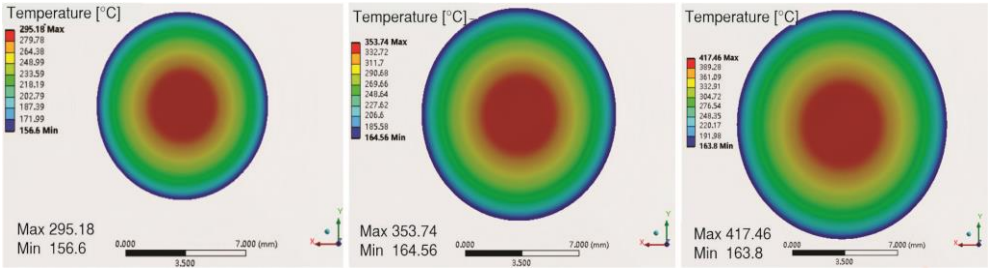

Figure 5. Temperature fields at the center of the dry patch under the Case 1 condition in the radiuses of 5 mm, 6 mm, and 7 mm

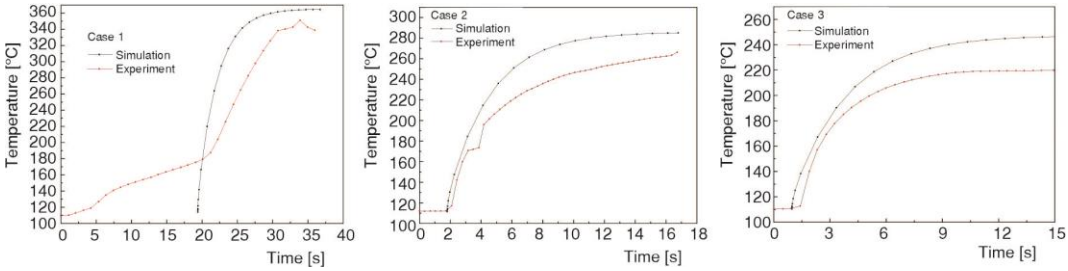

Figure 6. Cases 1-3 for the case of center temperature distribution *vs.* time for dry patch radius of 6 mm

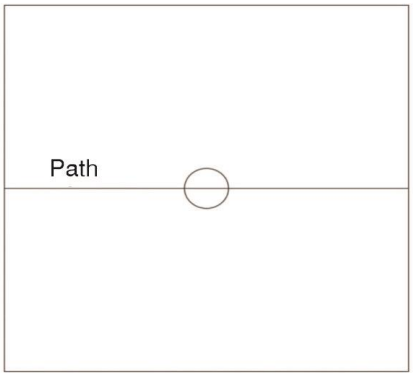

Figure 7. Schematic diagram of the scatter path

Stress calculation

The temperature data of Cases 1-3 for a dry patch radius of 6 mm was taken and imported into the stress calculation module of ANSYS Workbench. At the same time, the scatter plot was drawn in order to observe the distribution of the equivalent stress and temperature from the edge to the center. The path schematic is shown in the fig. 7.

In the absence of external constraints, the material undergoes free thermal expansion, and the stresses are only caused by the uneven temperatures in various parts of the material. The trend of stress distribution in Cases 1-3 is consistent, and the stresses reach the peaks of the stresses at the periphery and the center point of the simulated dry patches, respectively, and the schematic diagrams are shown in fig. 8.

As shown in fig. 9, in Cases 1-3, in the unconstrained case, the stress caused by the dry patch has exceeded the yield strength of the material itself, and the material will produce irreversible plastic deformation in the dry patch region, and at this time, the maximum temperature at the center point of the dry patch is far below the melting point of stainless steel.

Comparison and analysis

Considering that in practice the stainless steel base plate is screwed to the heated copper block, the equivalent force cases were also considered when no external constraints are

applied and when displacement constraints perpendicular to the direction of the stainless steel base surface are applied.

According to fig. 10, the trend of stress distribution observed in Cases 1-3 with bottom surface restraint applied is consistent: the stress values are higher at the periphery of the dry patches, while the stress values at the center point of the dry patches are significantly lower, and the maximum plastic deformation occurs at the periphery of the dry patches. The stress distribution due to thermal expansion of the material under the bottom surface confinement condition shows a different pattern and the magnitude of the stress values varies. In this case, as shown in fig. 11. Compared to the unconstrained case, the peak stresses near the periphery of the dry patch under bottom surface constraints were enhanced, but the value of the maximum stresses sustained by the material was slightly reduced, and the maximum stresses were concentrated at the periphery of the dry patch.

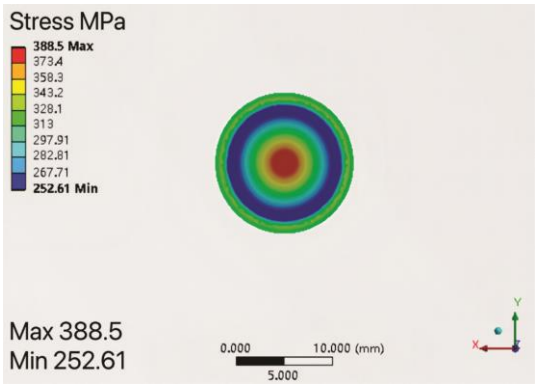

Figure 8. Stress distribution in the unconstrained case

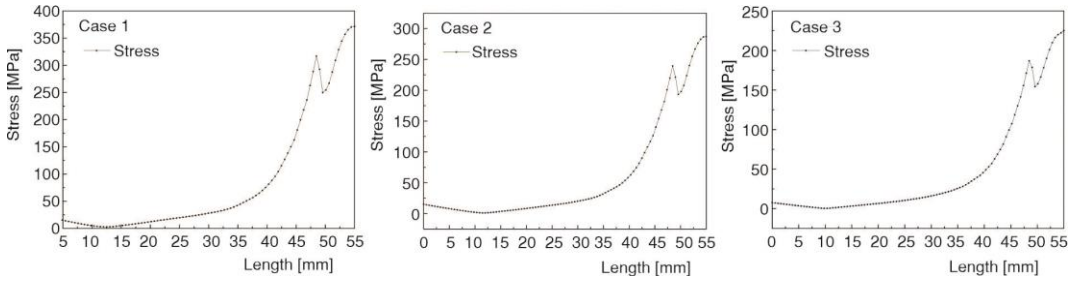

Figure 9. Equivalent stress distribution on path for the unconstrained case in Cases 1-3

The temperature distribution on the boiling surface is further analyzed. Figure 12 shows that the temperature gradient from the edge of the boiling surface to the center point of the dry patch increases and then decreases, and the maximum temperature gradient appears near the circumference of the dry patch. Since the heat transfer of the dry patch deteriorates after it is established on the wall, the area occupied by the dry patch heats up rapidly and the heat accumulated inside the region is transferred laterally by the plate material. It is reasonable to hypothesize that the large temperature gradient present at the circumference of the dry patch results in a stress peak on the circumference of the dry patch.

Sensitivity analysis

The thickness of stainless-steel plate

The stresses under different thicknesses at higher heat flux were investigated. Under the condition of no external constraints (based on the experimental data of Case 1, heat flux = 0.523 W/mm^2), the stress changes at the thickness of 1 mm and 10 mm of the stainless steel bottom are studied, respectively, and compared the results with the case of 2 mm, as shown in fig. 13. It can be observed that decreasing the thickness of the stainless steel base plate leads to

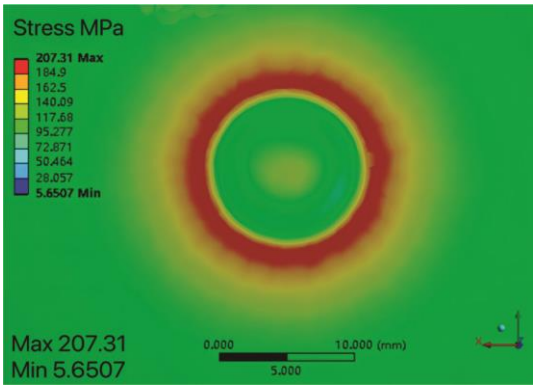

Figure 10. Equivalent stress distribution in the constrained case

an increase in the maximum temperature in the dry patch region. Especially in the case of a thin stainless steel base plate, the effect of reducing the thickness on the temperature in the dry patch region is more drastic. This is because the thinner plate has greater transverse heat resistance, which is not conducive to the heat transfer of the dry patch to the four sides.

Through the analysis of the stress situation, it can be found that the thinner stainless steel base plate will cause the temperature in the center of the dry patch to increase, and the stress suffered by the material increases

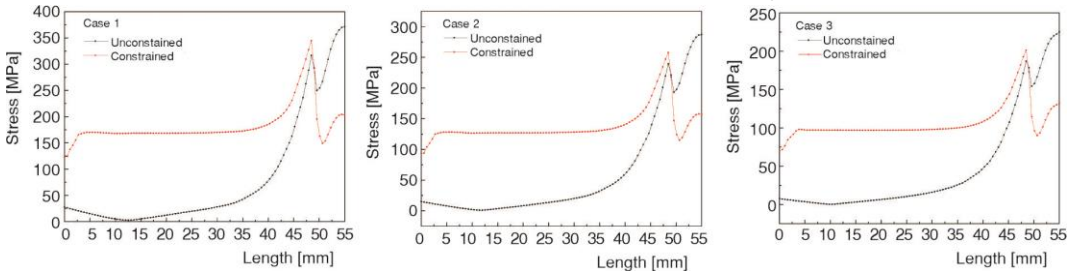

Figure 11. Equivalent stress distributions on path in Cases 1-3 with and without displacement constraints applied to the bottom surface

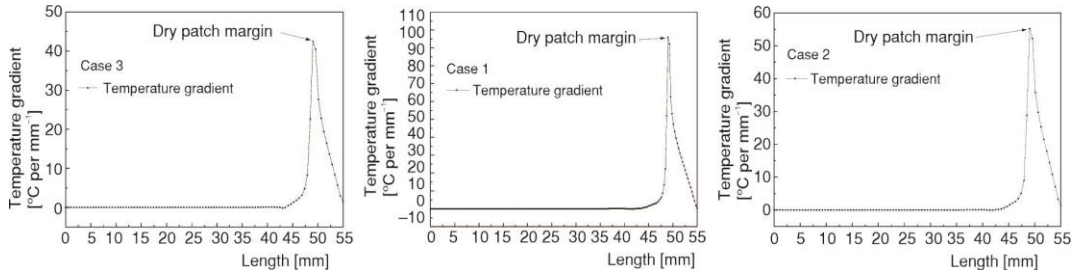

Figure 12. Temperature gradient on path for Cases 2-4

sharply, while in the case of thicker stainless steel walls, the stress peak near the circumference of the dry patch is closer to the stress peak in the center region of the dry patch. This indicates that the thicker stainless steel wall can distribute the stress more evenly, reducing the gradient of stress within the dry patch region, but the thicker stainless steel base plate will have a larger temperature difference within the heated plate material itself under the same heat flux, as shown in fig. 14. Therefore, under the condition of higher heat flux, selecting the appropriate thickness of the stainless steel bottom plate may help to mitigate the stress concentration without making the temperature difference inside the stainless steel too large.

Location of dry patch

Analyze the variation in material stress distribution as the dry patch approaches the edge of the boiling surface. Figure 15 illustrates the distance ‘a’ from the center of the dry patch

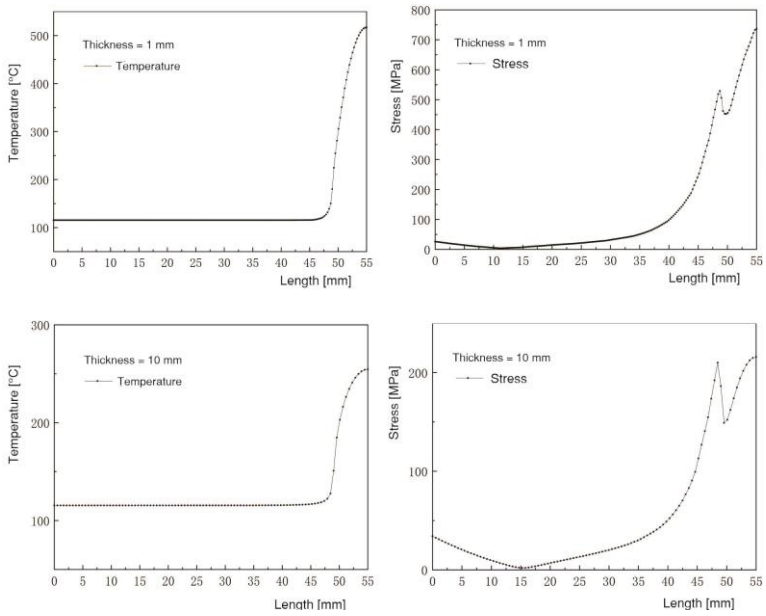

Figure 13. Temperature and equivalent stress distribution on path for thicknesses of 1 mm and 10 mm

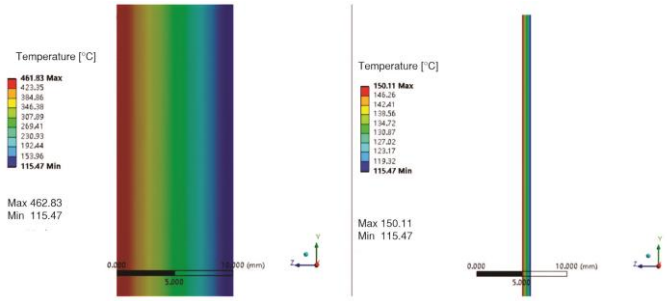

Figure 14. Steady-state temperature distribution before dry patch generation for thicknesses of 10 mm and 1 mm, respectively

circle to the edge of the boiling surface. The stress data point trajectory intersects the center of the dry patch circle. The dry patch stress distribution is considered for a = 15 mm, 20 mm, 25 mm, and 30 mm.

Figure 16 demonstrates significant stress concentration at the boiling surface edge when the dry patch center is positioned 10 mm, 15 mm, 20 mm, and 25 mm away. However, when the dry patch center is at a 30 mm distance from the boiling surface edge, the stress concentration effect at the edge is negligible. It is deduced that the stress influence range of the dry patch does not extend beyond five times its radius. This principle aids researchers in defining the computational domain.

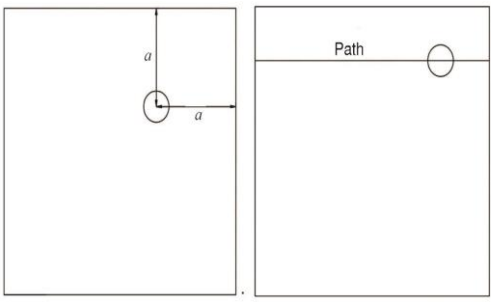

Figure 15. Schematic of dry patch locations and data point path

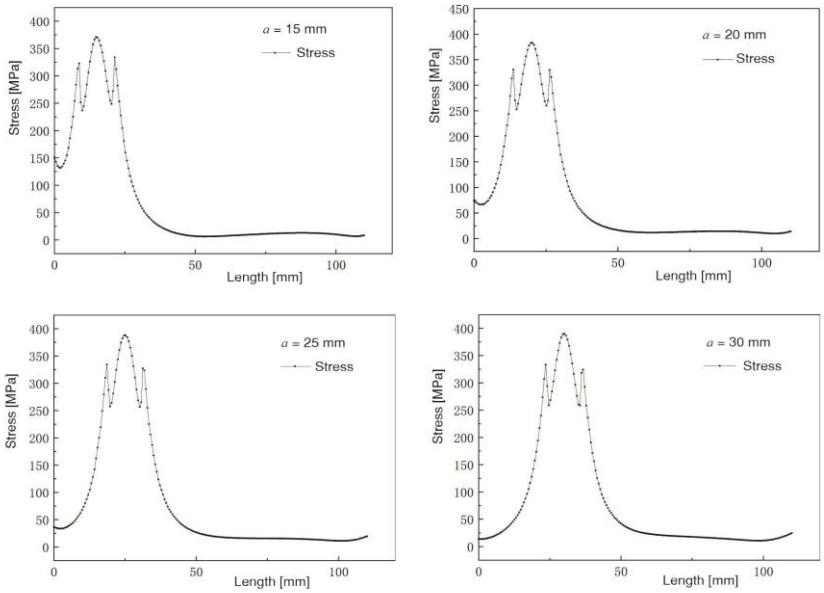

Figure 16. Equivalent stress distribution at a = 15 mm, 20 mm, 25 mm, and 30 mm

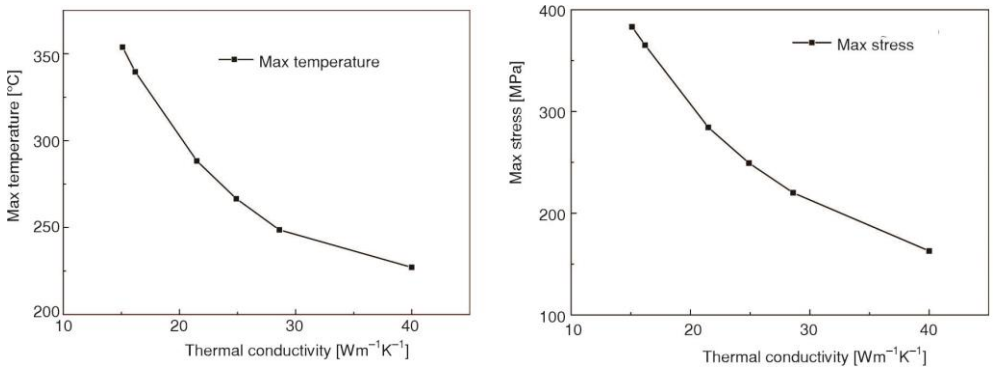

Figure 17. The maximum temperature and maximum stress of dry patch varying with thermal conductivity

Influence of thermal conductivity

Stainless steel, a crucial engineering material, exhibits a range of properties. The thermal conductivity of stainless steels typically ranges from 14 W/m/K to 45 W/m/K, indicating significant variability. Furthermore, the coefficients of thermal expansion for stainless steels generally fall between 16 μm/m/K and 17 μm/m/K, the specific heat capacities range from 0.46 kJ/kg/K to 0.51 kJ/kg/K, the Poisson's ratios range from 0.27 to 0.31, and the Young's moduli range from 190 GPa to 220 GPa. The thermal conductivity of stainless steel varies significantly varies among these properties, with a range spanning a factor of three, highlight the importance of considering thermal conductivity. A thermal conductivity of 15.1 W/m/K for stainless steel was utilized in the simulations, followed by analyses with constant material properties except for varying thermal conductivity, including simulations for thermal conductivities of 16.2

W/m/K, 21.5 W/m/K, 24.9 W/m/K, 28.6 W/m/K, and 40.0 W/m/K. The results, depicted in fig. 17, demonstrate that thermal conductivity primarily influences the maximum stress by affecting the maximum temperature within the dry patch: An increase in thermal conductivity correlates with a decrease in both the maximum temperature within the dry patch and the equivalent stress experienced by the material. Stainless steel materials exhibiting higher thermal conductivity offer increased advantages.

Conclusions

This study investigates thermal stress on wall surfaces during the occurrence of dry patches, employing experimental and simulation methods based on the dry patch model. The key findings are:

- Higher heat flux results in a rapid temperature increase within dry patches, causing localized maximum temperatures. This temperature difference induces thermal stresses that exceed the material's yield strength, potentially leading to irreversible plastic deformation or stress-induced fracture before melting.
- Significant stress peaks near dry patch edges, regardless of external constraints, indicate plastic deformation and increased wall superheating at these edges, contributing to dense bubble nucleation nearby. This complexity warrants further investigation in future studies.
- By reducing the thickness of stainless steel base plate, maximum dry patch temperatures increase, especially pronounced with thinner base plates, leading to sharp rises in thermal stresses within the material. In contrast, thicker walls mitigate the impact of thickness on stress.
- Thermal conductivity primarily affects maximum stress through its impact on the dry patch maximum temperature; higher conductivity can reduce stress levels.

The study deliberately sets the dry patch size to demonstrate CHF damage arising from thermal stress rather than just high temperature. Determining the size of dry patches reasonably is a focus of future work.

Acknowledgment

The authors would like to thank the Nuclear Power Institute of China under Grant No. JDYY Ⅱ-05-FWHT-GKJT-2022028 for financial support of this work.

Reference

[1] Kutateladze, S., On the Transition to Film Boiling Under Natural Convection, *Kotloturb.*, *3*. (1948), p. 10
[2] Zuber, N., *Hydrodynamic Aspects of Boiling Heat Transfer*, United States Atomic Energy Commission, Technical Information Service, Rockville, Md., USA, 1959
[3] Haramura, Y., Katto, Y., A New Hydrodynamic Model of Critical Heat Flux, Applicable Widely to Both Pool and Forced Convection Boiling on Submerged Bodies in Saturated Liquids, *International Journal of Heat and Mass Transfer*, *26* (1983), 3, pp. 389-399
[4] Ha, S. J., No, H. C., A Dry-Spot Model for Transition Boiling Heat Transfer in Pool Boiling, *International Journal of Heat and Mass Transfer*, *41* (1998), 23, pp. 3771-3779
[5] Ha, S. J., No, H. C., A Dry-Spot Model of Critical Heat Flux in Pool and Forced Convection Boiling, *International Journal of Heat and Mass Transfer*, *41* (1998), 2, pp. 303-311
[6] Tachibana, F., *et al.*, Non-Hydrodynamic Aspects of Pool Boiling Burnout, *Journal of Nuclear Science and Technology*, *4* (1967), 3, pp. 121-130
[7] Costello, C. P. A Salient Nonhydrodynamic Effect on Pool Boiling Burnout of Small Semicylindrical Heaters, *Chemical Engineering Progress, Symposium Series*, *61* (1965), 57, pp. 258-268
[8] Howard, A., Mudawar, H. I., Orientation Effects on Pool Boiling Critical Heat Flux (CHF) and Modeling of CHF for Near-Vertical Surfaces, *International Journal of Heat and Mass Transfer*, *42* (1999), 9, pp. 1665-1688

[9] Van Ouwerkerk, H., Burnout in Pool Boiling the Stability of Boiling Mechanisms, *International Journal of Heat and Mass Transfer*, *15* (1972), 1, pp. 25-34
[10] Unal, C., *et al.*, Unifying the Controlling Mechanisms for the Critical Heat Flux and Quenching: The Ability of Liquid to Contact the Hot Surface, *Journal of Heat Transfer*, *114* (1992), 4, pp. 972-982
[11] Gong, S., *et al.*, An Experimental Investigation on Bubble Dynamics and Boiling Crisis in Liquid Films, *International Journal of Heat and Mass Transfer*, *79* (2014), Dec., pp. 694-703
[12] Chu, I.-C., *et al.*, Visualization of Boiling Structure and Critical Heat Flux Phenomenon for a Narrow Heating Surface in a Horizontal Pool of Saturated Water, *International Journal of Heat and Mass Transfer*, *62* (2013), July, pp. 142-152
[13] Chu, I.-C., *et al.*, Observation of Critical Heat Flux Mechanism in Horizontal Pool Boiling of Saturated Water, *Nuclear Engineering and Design*, *279* (2014), Nov., pp. 189-199
[14] Bernardin, J. D., Mudawar, I., The Leidenfrost Point: Experimental Study and Assessment of Existing Models, *Journal of Heat Transfer*, *121* (1999), 4, pp. 894-903
[15] Choi, J. Y., *et al.*, Development of a Dry Patch Model for Critical Heat Flux Prediction, *International Journal of Heat and Mass Transfer*, *100* (2016), Sept., pp. 386-395
[16] Liter, S. G., Kaviany, M., Pool-Boiling CHF Enhancement by Modulated Porous-Layer Coating: Theory and Experiment, *International Journal of Heat and Mass Transfer*, *44* (2001), 22, pp. 4287-4311
[17] Theofanous, T., *et al.*, The Boiling Crisis Phenomenon: Part I: Nucleation and Nucleate Boiling Heat Transfer, *Experimental Thermal and Fluid Science*, *26* (2002), 6-7, pp. 775-792
[18] Theofanous, T., *et al.*, The Boiling Crisis Phenomenon: Part II: Dryout Dynamics and Burnout, *Experimental Thermal and Fluid Science*, *26* (2002), 6-7, pp. 793-810
[19] Kim, D. E., *et al.*, Simultaneous Observation of Dynamics and Thermal Evolution of Irreversible Dry Spot at Critical Heat Flux in Pool Boiling, *International Journal of Heat and Mass Transfer*, *99*. (2016), Aug., pp. 409-424
[20] Qin, H., *et al.*, Analysis of the Oscillation in the System of Parallel Narrow Channels, *Annals of Nuclear Energy*, *168* (2022), 108906

Paper submitted: March 24, 2024
Paper revised: June 12, 2024
Paper accepted: June 14, 2024